IEEE Access
Multidisciplinary ⋮ Rapid Review ⋮ Open Access Journal

Received 19 December 2023, accepted 13 January 2024, date of publication 17 January 2024,
date of current version 25 January 2024.

Digital Object Identifier 10.1109/ACCESS.2024.3355131

RESEARCH ARTICLE

Control Strategy and Implementation of Seamless Closed-Loop Load Transfer Mobile Prototype for 400 V Distribution Network

ZHITAO GUAN[1], PENGFEI TANG[1], CHENGXIONG MAO[1], (Fellow, IEEE), DAN WANG[1], (Senior Member, IEEE), LEXIANG WANG[1], WENGE LIU[1], MIAOMIAO DU[1], JUNLIN LI[2], AND XIAOCONG WANG[2]

[1]School of Electrical and Electronic Engineering, Huazhong University of Science and Technology, Wuhan 430074, China
[2]Guangzhou Power Supply Bureau, Guangzhou Power Grid Company Ltd., Guangzhou 510699, China

Corresponding author: Dan Wang (wangdan@mail.hust.edu.cn)

This work was supported by the Science and Technology Project of China Southern Power Grid Corporation, under Grant GZHKJXM20190024.

ABSTRACT Recently, ordinary residential users' tolerance for power outages has dropped much by the flourishing economy. To further improve the power supply reliability, a scheme of seamless closed-loop load transfer was proposed based on series compensation technology. For its field application, two points should be considered: 1) For the efficient utilization, the device is designed with high mobility. But its mobility is limited due to its power requirements and the usage of magnetic components. 2) The mobility leads to variable nodes interconnected each time, which puts forward high requirements for the control strategy. The following are proposed: 1) Proposing a novel control strategy based on online impedance estimation method to ensure the effectiveness of the mobile prototype in variable scenarios. 2) Employing modular design and series-parallel mode to reduce the individual cabinet's volume, while utilizing the short-term overload capacity of magnetic components to augment the power density. A mobile prototype is developed, and test results prove the effectiveness of the control strategy and the engineering feasibility of the prototype.

INDEX TERMS Interconnected power system, online impedance estimation, power distribution reliability, series-parallel mode.

I. INTRODUCTION

A. PROBLEM DEFINITION

With the economic development in recent years, the power grid is developing rapidly into the smart grid. Security and reliability are the keys to build an intelligent distribution network [1], [2], [3]. It is necessary to undertake a large number of maintenance and transformation work of power system facilities to meet ever-increasing power demand securely [3]. Some essential customer loads cannot tolerate power supply interruptions and equips with an uninterruptible power supply (UPS) system [4]. However, the ordinary residential users without UPS have significantly diminished their capacity to endure power interruptions due to the flourishing economy [5]. Hence, the uninterrupted power supply operation (UPSO) is the key to improve the power supply reliability, and the UPSO's frequency is gradually increased by power supply companies [6].

The temporary power supply for low-voltage UPSOs can be from distributed power sources [7], [8] and near 400 V feeders. The UPSO, whose power supply is from near feeders, is called loop closing operation [9]. In China, distribution networks adopt a power supply mode with closed-loop design and open-loop operation [10], and the network structure is radial [11], which provides the basis for loop closing operation.

Due to the voltage difference between the bus bars of two power supply, loop closing operation causes impulse current

The associate editor coordinating the review of this manuscript and approving it for publication was Ali Raza.

and steady-state circulating current, both of which pose a threat to the safety of the power system [9], [10], [11]. The current researches mainly focus on establishing a loop closing model, evaluating the risks associated with loop closing, and mitigating the hazards presented by loop closing within the 10 kV distribution network [12], [13]. The loop closing devices for the 10 kV distribution network are developed in [14], [15], [16], but only key substations whose space meets the requirements can install the loop closing device. Hence, it is a challenge to solve the temporary power outages of most ordinary customers by the loop closing operation in the 10 kV distribution network, especially in the case of the maintenance of the 10 kV: 0.4 kV transformers.

The loop closing devices designed for the 0.4 kV distribution network are superior in volume, weight and cost. However, due to the large number of 0.4 kV nodes and the temporality of power outages (lasting 4-8 hours), the utilization of fixed devices is economically unviable. In [6], a mobile contact box was designed. The voltage amplitude and phase angle differences for allowing loop closing operation are set to 15 V and 5°, which are determined based on the engineer's knowledge and experiences. In [17], a scheme of seamless closed-loop load transfer (SCLT) was proposed based on power electronic technology, which has better performance in the impulse and steady-state circulating current. The SCLT devices can reduce the risk of loop closing operation and improve the power supply reliability [18].

The SCLT device will contribute to an increased cost, but a certain number of mobile SCLT devices can cover the whole area to meet the demand for power supply reliability. Hence, the increased cost of the mobile SCLT device is worth for improving power supply reliability. However, two 0.4 kV nodes connected by the device each time are generally different. It means that the upper-level grid and lower-level load are different. Hence, the design of SCLT system should adapt to variable scenarios, especially its control strategy, volume, and weight.

B. BACKGROUND OUTLOOK

1) CONTROL STRATEGY

Few papers study the control strategy of SCLT scheme [11], [17]. The simple PI and PR controllers are adopted in their control strategies. However, the control strategies are for the fixed system and ignore the impedance between the two substations.

Moreover, the control strategy of one process in SCLT scheme is similar to that of UPFC, so the control strategies of UPFC can be considered. The control strategies of UPFC can be divided into control strategy based on simple PI controller [19], feedback linearization [20], [21], [22], intellectual technology (such as, neural network and fuzzy controller [23], [24], [25]). The simple PI control strategy is often applied in engineering. However, because the *X/R* ratio of distribution network is smaller and more complex than that of transmission network, the simple PI controller cannot meet the requirements of SCLT system. The control strategies based on feedback linearization are mainly based on the fixed UPFC system, that is, the system impedance value can be measured offline [22]. The control strategies based on intellectual technology have better performance, but its implementation in the SCLT system requires a lot of data and accumulated experience.

2) VOLUME AND WEIGHT

SCLT circuit shares similar topology to unified power-flow controller (UPFC) and unified power quality conditioner (UPQC). The volume and weight of transformer accounts for 40% and 90% of the UPF/QC system [26]. To reduce the volume and weight, transformer-less UPF/QCs [26], [27] and UPFCs based on high-frequency transformer [19] are proposed. However, such topologies handle the full rated line voltage which typically requires a complex configuration. It is challenging to popularize their application in engineering.

C. CONTRIBUTIONS OF THIS WORK

The main aim of this work is to improve the convenience in engineering and the adaptability to variable scenarios of SCLT system. The following are some of the main contributions that can be derived from this body of work:

- An optimized control strategy based on online impedance estimation method is proposed. The impedance value of the upper power grid is predicted according to the information measured online, and is updated by the recursive least square estimation method. The proposed control strategy ensures the effectiveness of the mobile prototype in variable scenarios.
- The numerical model of the temperature field of the transformer is established. The relationship between the overload coefficient and the allowable overload time, volume and weight is analyzed, and then the value of overload coefficient is determined to be five.
- A mobile prototype is developed based on the SCLT scheme, which utilizes the overload capacity of magnetic components to reduce its volume and weight. The series-parallel operation of the modules is realized.
- Five cases are proposed, and the results verify the effectiveness of the control strategy and the engineering feasibility of the prototype.

D. PAPER LAYOUT

The remaining sections in this paper are arranged as follows. Section II shows the operation principle, the difficulties, and the corresponding solutions of SCLT system. Section III describes the basis for the determination of short-term overload coefficient of magnetic elements. Section IV illustrates the topology and main circuit of the SCLT prototype. Section V depicts the control system. Section VI provides the results of five cases and a discussion. The conclusions of this paper are outlined in section VII.

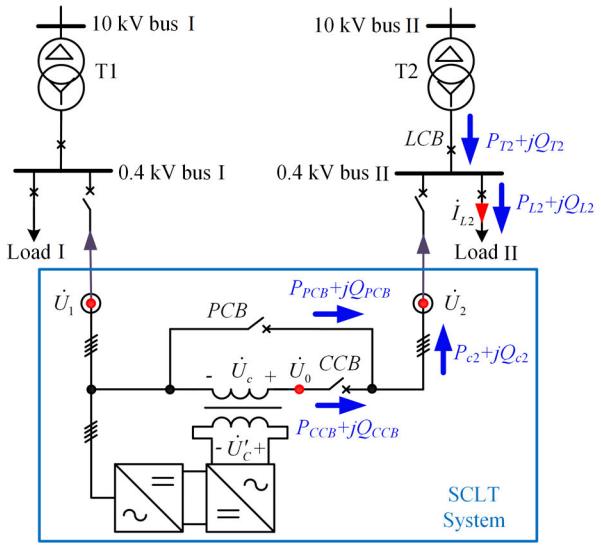

FIGURE 1. Schematic diagram of the SCLT system.

II. CONFIGURATION

The developed prototype will be applied to the scenarios where the 10 kV: 0.4 kV transformer is planned for maintenance or transformation. For example, the transformer T2 in Fig. 1 is planned for maintenance, and the voltage difference between bus I and bus II is so large that the normal loop closing operation is forbidden. On the day preceding the operation, the developed prototype will be relocated to the field and connected to two bus bars using temporarily installed cables. The next day, the prototype is capable of transferring the load II from bus II to bus I, a process referred to as power supply transferring operation. After the maintenance work (4)-8 hours), the prototype will restore the load II back to bus II, which is called power supply restoring operation. It is noted that there will be no momentary power outages in the load II during the above operations.

Fig. 1 illustrates a schematic diagram of the seamless closed-loop load transfer (SCLT) system. The voltages of bus I and bus II are signed as $\dot{U}_1$ and $\dot{U}_2$. There are two kinds of converters in the SCLT system. One is rectifier, and its function is to maintain DC voltage stability and provide power for the back-end inverter. The other is inverter, which can generate controllable voltage $\dot{U}'_c$ and inject the voltage $\dot{U}_c$ between two bus bars by series transformers. The $\dot{U}_0$ is the voltage after compensation, which is obtained by $\dot{U}_0 = \dot{U}_1 + \dot{U}_c$. Two converters work together to achieve the power supply transferring operation and power supply restoring operation.

The power supply transferring operation can be divided into four processes: the access process, power flow process, bypass process, and power self-circulation process.

- The aim of the access process is, that the closed-loop circuit breaker (*CCB*) is switched on when the voltage at both ends of the *CCB* is near ZERO. So, the SCLT system controls the injected voltage $\dot{U}_c = \dot{U}_2 - \dot{U}_1$.
- The aim of the power flow process is, that the load circuit breaker (*LCB*) is switched off when the transformer power $P_{T2} + jQ_{T2}$ is near ZERO. So, the SCLT system is in current mode, and the power $P_{c2} + jQ_{c2}$ transmitted into bus II will be controlled to follow the load II power $P_{L2} + jQ_{L2}$.
- The aim of the bypass process is, that the prototype bypass circuit breaker (*PCB*) is switched on when the voltage at both ends of the *PCB* is near ZERO. So, the SCLT system controls the injected voltage $\dot{U}_c = 0$.
- The aim of the power self-circulation process is, that the *CCB* is switched off when the power $P_{CCB} + jQ_{CCB}$ is near ZERO. So, the SCLT system is in current mode, and the power $P_{PCB} + jQ_{PCB}$ will be controlled to follow the load II power $P_{L2} + jQ_{L2}$.

The power supply restoring operation also includes four processes: assess process, power self-circulation process, voltage regulation process, and power flow process. The SCLT prototype plays the role of a temporary transfer interface.

Based on series compensation technology, the developed SCLT system shows exceptional capacity in achieving both the power supply transferring operation and the power supply restoring operation. In the scenario where the voltage phase angle difference is less than 60°, compared with the back-to-back full power conversion scheme [28], the adopted scheme is superior in the power capacity [16]. Moreover, when a fault occurs in the grid, the adopted scheme is more reliable due to the isolating transformer. However, there are following difficulties to develop the mobile SCLT prototype:

1) MOBILITY

The developed prototype will be used in the 0.4 kV grid. The road between residential buildings is narrow and uneven, and it puts forward high requirements for device mobility. Moreover, the addition of the series transformers increases the volume and weight [29].

2) VARIABLE SCENARIOS

The prototype is mobile, and two 0.4 kV nodes connected by the device each time are generally different. It means that the upper-level grid and lower-level load are different, specifically embodied in the equivalent power source and equivalent impedance between the two bus bars, as well as the characteristics of load current [30].

3) SUBSTATION SITUATION

For the control strategy of power flow process in the power supply transferring operation and the voltage regulation process in the power supply restoring operation, it is indispensable to obtain the information about the currents flowing through the *LCB* and the voltages between the *LCB*, respectively. Besides, there is no switching state return signal on the *LCB* in some substations, especially in the urban village area. Hence, the additional measuring unit is required.

Accordingly, the following solutions are proposed:

a: SHORT-TERM OVERLOAD CAPACITY

The power supply transferring operation and power supply restoring operation can be completed in 60 seconds because of the high flexibility of power electronic devices, and then the prototype will be bypassed. On the other hand, it is safe for the magnetic components to flow through 5-6 times the rated current for 60 seconds, which is called the short-term overload capacity of the magnetic components. So, the rated current of magnetic components can be set to one fifth of the maximum current, and their volume and weight can be greatly reduced.

b: ONLINE IMPEDANCE ESTIMATION METHOD

The equivalent impedance between the two bus bars is directly related to the power flow process. The framework of distribution network is complex, and the equivalent impedance is difficult to obtain. Therefore, an online impedance estimation method is proposed. The impedance value of the upper power grid is predicted according to the information measured online, and is updated by the recursive least square estimation method.

c: MODULAR DESIGN AND SERIES-PARALLEL MODE

The modular design is adopted to reduce the volume and weight of a single cabinet. Moreover, the series and parallel mode are designed to expand the voltage and current adaptation range of the prototype, respectively. In this way, the capacity and voltage requirements of variable scenarios are met by series-parallel connection of different numbers of modules.

d: REMOTE MEASURING UNIT

To obtain the information about the current flowing through the *LCB* and the voltages between the *LCB*, the remote measuring unit (RMU) is designed. The voltage and current information are collected and transmitted to the SCLT prototype by RMU. Its communication mode is wireless communication. Moreover, RMU also has the function of indicating the operator to switch the *LCB*.

III. SHORT-TERM OVERLOAD CAPACITY

Currently, there are few papers to study the overload operating conditions of magnetic components (such as dry-type transformer) more than three times [31]. Hence, the numerical model of the temperature field of the magnetic element is established for research. In order to determine the overload coefficient of magnetic components, the relationship between overload coefficient and overload time, weight and volume is studied. The series transformer is used as the thermal analysis component below.

Since the rated voltage and operating current of the transformer are determined, the cross-sectional area of the core and the number of winding turns are also determined. The overload coefficient will directly lead to the change of the cross-sectional area of the winding wire, and then the core size and the spatial distribution of the winding will be changed correspondingly.

A. LOAD LOSS

The wire adopts copper wire. After determining the current density, the cross-sectional area of the wire can be obtained.

$$s = \frac{I}{n \cdot J} \tag{1}$$

where I is the maximum operating current of the winding wire, n is the overload coefficient, and J is the set current density.

According to the spatial distribution of the winding, the length of the winding wire can be obtained, and then the wire resistance value can be obtained.

$$R = \frac{\rho \cdot l}{s} \tag{2}$$

where l is the length of the winding wire, and ρ is the resistivity of copper.

Thus, the load loss of the winding is obtained [32].

$$\begin{cases} P_r = K_w \cdot I^2 \cdot R \\ K_w = 3.8 \left(\dfrac{234.5 + 75}{234.5 + T} \right)^2 \left(\dfrac{f \cdot W \cdot a \cdot s \cdot \rho_\sigma}{h} \right)^2 \times 10^{-7} \end{cases} \tag{3}$$

where K_w is the vortex loss coefficient, T is the winding temperature, f is the current frequency, a is the conductor radial dimension, ρ_σ is the leakage coefficient, and h is the equivalent height of winding.

B. HEAT TRANSFER

The heat transfer mainly considers two point: convective and radiative heat transfer [33]. For convective heat transfer, a qualitative temperature needs to be determined first. Then, according to the qualitative temperature, the physical properties of the air at the corresponding temperature can be obtained by looking up the table, such as thermal conductivity λ_m, Motion consistency υ_m, and Prandtl value Pr_m. Then, the Grashof value can be obtained.

$$Gr_m = \left(\frac{g \cdot \beta \cdot \Delta T \cdot h^3}{\upsilon^2} \right)_m \tag{4}$$

where g is the gravity acceleration value, β is the coefficient of thermal expansion of air, and ΔT is the temperature difference value.

For the convective heat transfer between the outer winding and the air, and between the inner and outer windings, the Nusselt values are expressed as (5) and (6), respectively.

$$Nu_{1\text{-}0} = \left\{ 0.825 + \frac{0.387 \left(Gr \cdot Pr \right)^{1/6}}{\left[1 + \left(0.492 / Pr \right)^{9/16} \right]^{8/27}} \right\}^2 \tag{5}$$

$$Nu_{1\text{-}2} = 0.54 \left(Gr \cdot Pr \right)^{1/4} \tag{6}$$

Then, the heat transfer coefficient per unit area and the convective heat transfer power can be expressed as (7) and (8), respectively.

$$h_{heat} = Nu \cdot \lambda_m / h \tag{7}$$

$$\Phi = h \cdot S_j \cdot \Delta T \tag{8}$$

where S_j is the effective heat exchange area.

For radiative heat transfer, the emissivity ε of the winding is set to 0.9. Then the radiative heat transfer power can be expressed as (9).

$$Q_{1\text{-}2} = C_{1\text{-}2} \cdot \varphi_{1\text{-}2} \cdot S_j \left[\left(\frac{T_1}{100} \right)^4 - \left(\frac{T_2}{100} \right)^4 \right] \tag{9}$$

where C_{1-2} and φ_{1-2} are the angular coefficient and total radiation coefficient, respectively.

For the radiative heat transfer between the outer winding and the air, and between the inner and outer windings, the angular coefficient and total radiation coefficient are expressed as (10) and (11), respectively.

$$\begin{cases} \varphi_{1\text{-}0} = 1.0 \\ C_{1\text{-}0} = C_0 \cdot \varepsilon_1 \end{cases} \tag{10}$$

$$\begin{cases} \varphi_{1\text{-}2} = 1.0 \\ C_{1\text{-}2} = \dfrac{C_0}{\left[\frac{1}{\varepsilon_1} + \frac{S_{jn1}}{S_{jw2}} \left(\frac{1}{\varepsilon_1} - 1 \right) \right]} \end{cases} \tag{11}$$

where C_0 is the radiation coefficient of blackbody (5.67 W/(m^2· K^4)).

C. TEMPERATURE RISE

According the load loss and heat transfer, the temperature rise [34] can be calculated by (12).

$$P_k \mathrm{d}t = cM \mathrm{d}\tau + \Phi \mathrm{d}t + \sum Q \mathrm{d}t \tag{12}$$

where dt is the time step, c is the specific heat capacity of the winding, M is the quality of winding, and dτ is the temperature rise.

D. RESULT ANALYSIS

The transformers with different overload coefficients are designed [32], and the results about the weight, volume, and temperature rise are shown in Table 1. In Table 1, W_{Fe}, W_{Cu} and W_{Fe+Cu} are the weight of the core, the winding, and their sum.

Because of the high flexibility of power electronic devices, the time required for power supply transferring operation is less than 60 seconds. Then, a certain margin needs to be considered, and the overload coefficient should not be over 6.

Considering the weight, volume and the overload time, the overload coefficient can be set to 5-6. The overload coefficient of transformers in the SCLT prototype is set to 5. The weight and volume are 26.3 kg (including the components for fixing) and 5.1 m^3. In this way, the weight and volume of the series transformer can be reduced to 27.2% and 27.9%, respectively. The same way can also be applied to the filter inductors.

TABLE 1. The calculation results of the single-phase transformer.

n	Time required for the winding temperature to reach T°C /s			Winding weight/kg			Volume /m^3
	T=125	T=135	T=145	W_{Fe}	W_{Cu}	W_{Fe+Cu}	
1	/	/	/	**32.1**	**52.5**	**84.6**	**19.0**
2	800.5	883.9	965.9	17.9	28.2	46.1	10.7
3	366.2	403.3	439.6	15.8	18.0	33.8	8.3
4	207.9	228.8	249.2	14.0	12.5	26.5	6.0
5	133.5	146.9	159.9	**13.2**	**9.8**	**23.0**	**5.3**
6	92.9	102.1	111.2	12.6	8.1	20.6	4.8
7	68.3	75.1	81.8	12.1	6.8	18.9	4.4
8	52.3	57.5	62.6	11.7	5.9	17.6	4.2
9	41.3	45.4	49.5	11.4	5.2	16.6	3.9

Note: The calculated volume only considers the core and windings. The room temperature is set to 40°C.

IV. TOPOLOGY AND MAIN CIRCUIT

To ensure mobility, the modular design is adopted. Those are series inverter (S-INV), parallel rectifier (P-REC), and RMU. A single S-INV is for the scenarios where the voltage phase angle differences between two bus bars does not exceed 15°, and the maximum transferred load current value is less than 250 A. Corresponding to Fig. 1, they are $|\angle \dot{U}_2 - \angle \dot{U}_1|$ and $|\dot{I}_{L2}|$, respectively. Besides, the allowable fluctuation range of grid voltage is ±7 %.

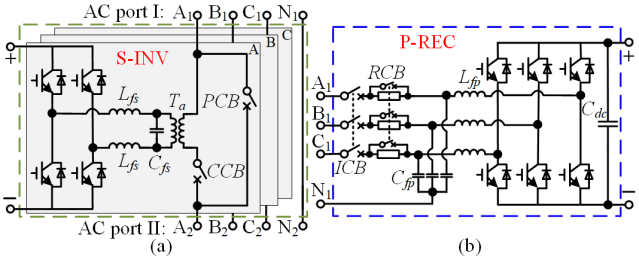

FIGURE 2. Topology. (a) Series inverter. (b) Parallel rectifier.

A. SERIES INVERTER

Because of the distribution network with high three-phase asymmetry, the three H-bridges structure is employed, as shown in Fig. 2(a). The S-INV can inject the voltages into two 0.4 kV AC bus bars through three single-phase series transformers. The S-INV is an inverter with controllable output voltage and enables four processes of the SCLT scheme by adjusting the injected voltage $\dot{U}_c$. The switching frequency is set to 5 kHz, and the unipolar frequency doubling SPWM method is used.

1) SERIES TRANSFORMER

The rated voltage phase angle differences of the SCLT prototype are set to 15°, and the allowable fluctuation range

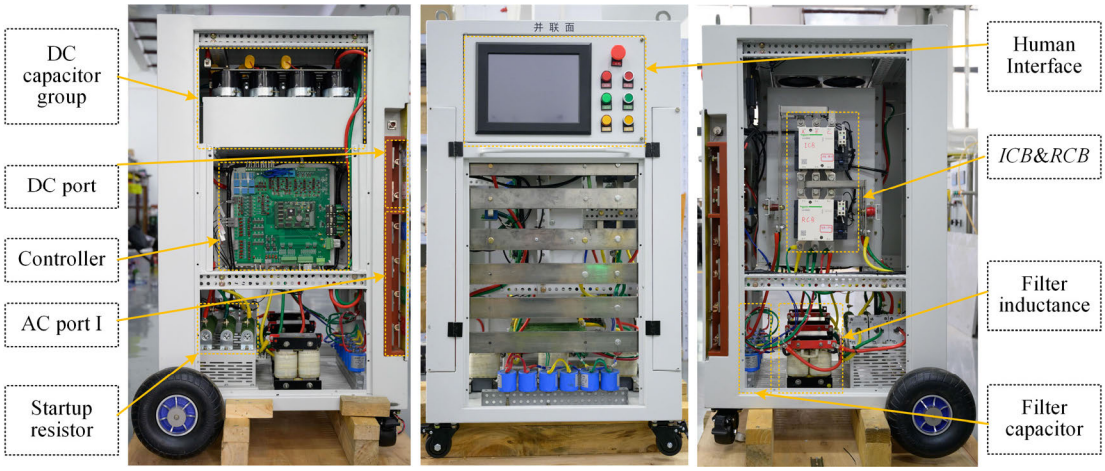

FIGURE 3. The mounting arrangement of the series inverter.

of grid voltage is ±7 %. This means that the injected single-phase voltage RMS should be at least 68.3 V. The rated value of DC voltage is set to 700 V. Hence, the ratio G of series transformers is set to 70 V:280 V.

The current-resistant of the low voltage side of the series transformers should be at least 250 A. Considering the short-term overload capacity of the magnetic components, the rated value is set to 50 A, and the rated capacity of series transformers is set to 3.5 kVA.

2) THREE-PHASE LC FILTER

A three-phase LC filter is adopted to suppress the influence of the high-frequency switching of IGBT. The model of the series transformer adopts a three-capacitor equivalent circuit model [35]. To suppress the influence on grid voltage by distributed capacitance, the filter inductance is split into two parts connected at the midpoint of the arm of the H-bridge, as shown in Fig. 2(a). The values of the filter capacitor C_{fs} and inductance L_{fs} are set to 39 μF and 1 mH, respectively. Similarly, the current-resistant of the filter inductance L_{fs} is 62.5 A, and the rated current is set to 12.5 A.

3) MOUNTING ARRANGEMENT

The S-INV's mounting arrangement is shown in Fig. 3. The cabinet size is $700(L)\times700(D)\times1100(H)$ mm^3, and its weight is about 220 kg. The DC and AC ports are installed on the column of the cabinet, which is convenient for operator wiring. The IGBTs and its drivers are installed behind the controller.

B. PARALLEL RECTIFIER

The P-REC is a rectifier with three-phase four-wire input and a three-phase LC *filter*. Its main circuit is shown in Fig. 2(b). Its functions are to maintain DC voltage stability and provide power to S-INVs, and power factor correction.

1) RATED CAPACITY

The rated capacity of P-REC depends on the active power required by S-INVs. In the case of a transferred load current value of 250 A, the active power required by a single S-INV can be calculated based on the load power factor, phase angle and amplitude values of two bus bars. The calculation results reveal a maximum active power value of 42.84 kW. The P-REC can provide power for two S-INVs in series mode or parallel mode. Besides, the injected voltage and transfer current cannot reach the maximum value simultaneously, so the P-REC's rated capacity is set to 85 kVA.

2) RATED DC VOLTAGE AND DC CAPACITOR

To reduce the mass and volume of the SCLT prototype, the 400 V:200 V three-phase transformer is not adopted. Hence, the rated value of DC voltage is set to 700 V.

The DC capacitor group C_{dc} has a withstand voltage of 900 V and a capacitance of 24 mF. It is composed of eight capacitors with a withstand voltage of 450 V and a capacitance value of 12 mF in series and parallel.

3) THREE-PHASE LC FILTER

A three-phase LC filter is adopted, and the power network neutral point is connected to the common point of filter capacitors. The value of filter capacitor C_{fp} and inductance L_{fp} are set to 50 V, respectively. The rated current of filter inductance L_{fp} is set to 30 A.

4) MOUNTING ARRANGEMENT

The P-REC's mounting arrangement is shown in Fig. 4. The cabinet size is $700(L)\times700(D)\times1100(H)$ mm^3, and its weight is about 150 kg.

C. REMOTE MEASURING UNIT

In practical engineering applications, the distance between the SCLT prototype and the substation, where the *LCB* (Loop Closing Breaker) is situated, can span the distance of a building. Since both operations require information regarding the currents flowing through the *LCB* and the voltages between the *LCB*, the design incorporates the use of an RMU, as shown in Fig. 5. The voltage probes and

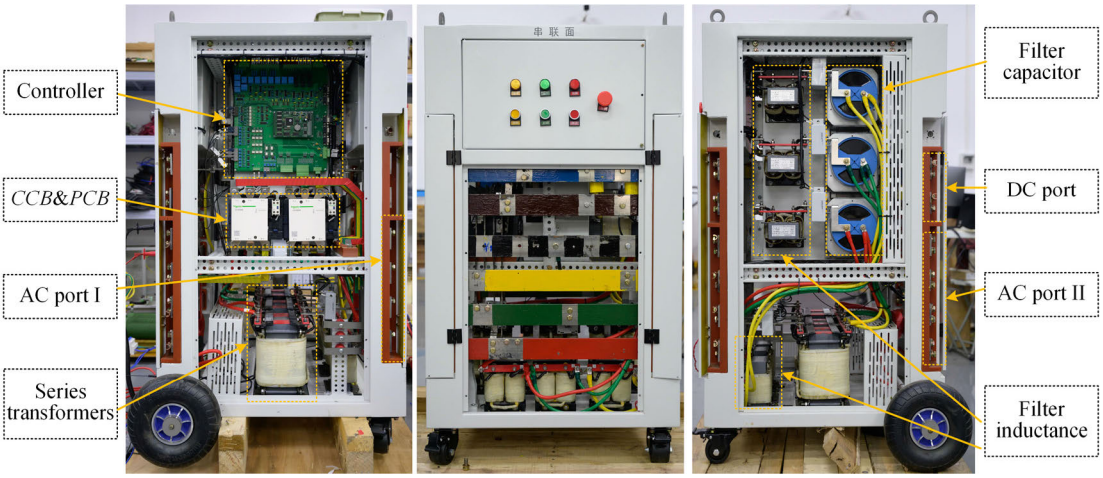

FIGURE 4. The mounting arrangement of the parallel inverter.

FIGURE 5. Components of remote measuring unit.

the open-loop Rogowski coils are adopted for temporary measurement. In this way, the three-phase currents flowing through the *LCB* and the voltages at each end of the *LCB* are measured. These measurements serve the purpose of the power flow control of the power supply transferring operation and the voltage regulation control of power supply restoring operation. Then the collected data is transmitted to the SCLT prototype by RMU's antenna. Moreover, the RMU features indicating lights on the controller's side, enabling the operator to conveniently switch the *LCB*. It is noted that the RMU is temporary, and the interval of information is updated at an interval of 100 ms.

V. CONTROL SYSTEM

The SCLT prototype, which involves two active converters and four operation processes, requires a dependable and optimized control system to achieve two operations and switching of four processes.

A. CONTROLLER STRUCTURE DESCRIPTION

As shown in Fig. 6, a hierarchical controller structure with digital signal processors (DSPs) and SGS-THOMSON microelectronics 32-bit microcontroller unit (STM 32) is employed to meet the demand of the SCLT prototype. The designed control system can be divided into three parts: primary DSP for P-REC, secondary DSP for S-INV, and STM 32 for RMU.

The primary DSP is responsible for the control strategy of P-REC and the overall control strategy of the four processes. In detail, the functions include the generation of IGBT triggering signals for P-REC, the calculation of data from secondary DSPs and RMU, and the generation of control variables for secondary DSPs. The primary functions of the secondary DSPs are to synthesize the reference voltage for four processes and generate the corresponding IGBT triggering signals for S-INVs. The STM 32 is utilized to wirelessly transmit the measured values to the primary DSP and instructions to operator B regarding the switching of the LCB. The information update time intervals between the primary DSP and the secondary DSPs as well as between the primary DSP and the RMU are set at 40 ms and 100 ms, respectively.

B. LOWER-LEVEL CONTROL STRATEGY

It is assumed that the phase angle of $\dot{U}_1$ is set to 0°, and the d- and q-axis component represent the component in phase with $\dot{U}_1$ and lagging phase 90° of $\dot{U}_1$, respectively.

1) FEEDFORWARD FOR LC FILTER

The injected voltage $\dot{U}_c$ and current $\dot{I}_c$ in the contact line can be measured. Then the d- and q-axis of voltage and current of series transformer on the LC filter side can be expressed as (13) and (14), respectively.

$$\begin{cases} U'_{cd} = U_{cd}/G \\ U'_{cq} = U_{cq}/G \end{cases} \tag{13}$$

$$\begin{cases} I'_{cd} = I_{cd} \cdot G \\ I'_{cq} = I_{cq} \cdot G \end{cases} \tag{14}$$

where U_{cd} and U_{cq}, I_{cd} and I_{cq} are d- and q-axis of voltage and current of series transformer on the grid side, respectively.

The d- and q-axis of the current injected into filter capacitance and current of filter inductor can be expressed as (15) and (16), respectively.

$$\begin{bmatrix} i_{C_{fs}d} \\ i_{C_{fs}q} \end{bmatrix} = \begin{bmatrix} C_{fs}s & -\omega C_{fs} \\ \omega C_{fs} & C_{fs}s \end{bmatrix} \begin{bmatrix} U'_{cd} \\ U'_{cq} \end{bmatrix} \tag{15}$$

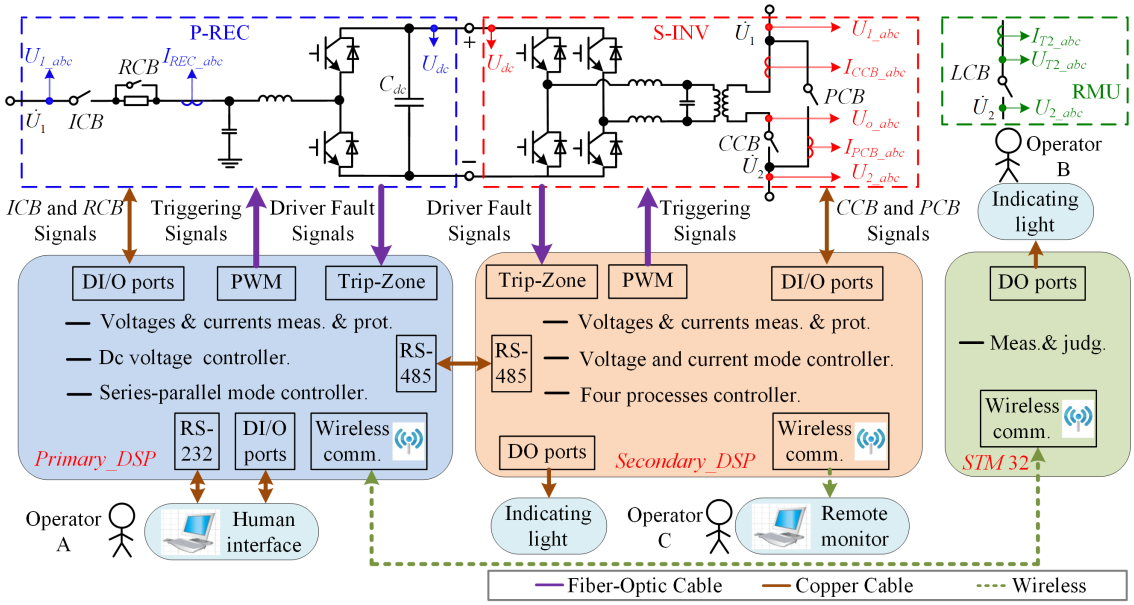

FIGURE 6. Detailed controller structure.

$$\begin{cases} i_{L_{fs}d} = i_{C_{fs}d} + I'_{cd} \\ i_{L_{fs}q} = i_{C_{fs}q} + I'_{cq} \end{cases} \tag{16}$$

The d- and q-axis of the equivalent voltage of H-bridge outlet can be expressed as (17).

$$\begin{bmatrix} e_{INV\_d} \\ e_{INV\_q} \end{bmatrix} = \begin{bmatrix} L_{fs}s & -\omega L_{fs} \\ \omega L_{fs} & L_{fs}s \end{bmatrix} \begin{bmatrix} i_{L_{fs}\_d} \\ i_{L_{fs}\_q} \end{bmatrix} + \begin{bmatrix} U'_{cd} \\ U'_{cq} \end{bmatrix} \tag{17}$$

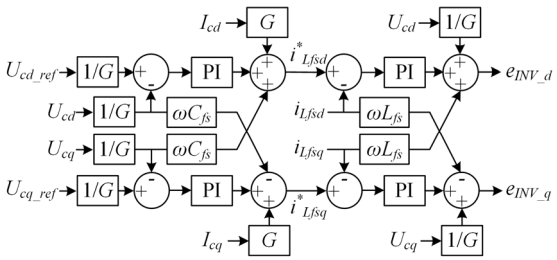

FIGURE 7. The inner-loop loop control strategy of S-INV.

The PI controllers are used to compensate the differential of voltage and current [20]. As shown in Fig. 7, the inner-loop control strategy of S-INV adopts PI controllers for voltage and current. In Fig. 7, U_{cd_ref} and U_{cq_ref}, I_{cd_ref} and I_{cq_ref} are d- and q-axis of reference values for $\dot{U}_c$ and $\dot{I}_c$, respectively.

2) POWER FLOW PROCESS

Once the prototype is connected into two bus bars, its primary objective is to control currents in the contact line. Due to the uncertain nature of the equivalent impedance between the two bus bars, only the simple PI controller and PI parameter fuzzy controller work. Their outer loop control strategies are shown in Fig. 8.

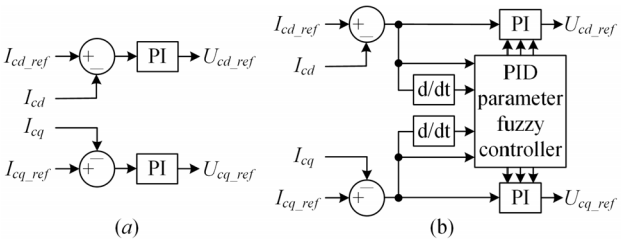

FIGURE 8. The outer loop control strategy. (a) Simple PI control strategy. (b) PI parameter fuzzy control strategy.

However, the small X/R ratio of the distribution network is smaller than that of the transmission network, the performance of simple PI control strategy is not so good. For the PI parameter fuzzy control strategy, the formulation of fuzzy rules for the SCLT system requires the experience of operators. Hence, an online impedance estimation method is proposed.

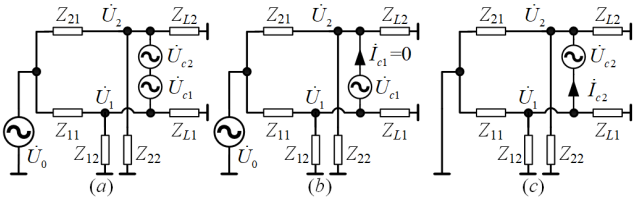

FIGURE 9. The equivalent circuit of SCLT system and grid. (a) $\dot{U}_{c1}+\dot{U}_{c2}$. (b) $\dot{U}_{c1}$. (c) $\dot{U}_{c2}$.

Fig. 9(a) is the equivalent circuit of Fig. 1, which is assumed that the transformer wiring groups are consistent. The $\dot{U}_0$ in Fig. 9 is the common point voltage of the upper grid of the two bus bars, which remains constant throughout the power flow process. Z_{11} and Z_{21} are the equivalent mutual

impedance of common point and bus I, common point and bus II, respectively. Z_{12} and Z_{22} are the equivalent mutual impedance of neutral point and bus I, neutral point and bus II, which does not include the load impedance of the corresponding bus. Z_{L1} and Z_{L2} are the load impedance of the bus I and bus II, respectively.

The SCLT prototype is equivalent to two voltage sources $\dot{U}_{c1}$ and $\dot{U}_{c2}$. The function of $\dot{U}_{c1}$ is to compensate the voltage difference between two bus bars, whose compensation current $\dot{I}_{c1}$ value is zero. The function of $\dot{U}_{c2}$ is to generate compensation current $\dot{I}_{c2}$ for power control. According to the superposition theorem, Fig. 9(a) can be decomposed into Fig. 9(b) and Fig. 9(c). For $\dot{U}_{c2}$ in Fig. 9(c), the impedance is $Z_{11}//Z_{12}//Z_{L1}+ Z_{21}//Z_{22}//Z_{L2}$, which can be expressed as (18).

$$Z_{11}//Z_{12}//Z_{L1} + Z_{21}//Z_{22}//Z_{L2} = R_{c2} + jX_{c2} = R_{c2} + j\omega L_{c2} \tag{18}$$

where R_{c2}, X_{c2} and L_{c2} are the equivalent resistance, reactance and inductance in Fig. 9(c), respectively.

The equivalent resistance and reactance can be expressed as:

$$\begin{bmatrix} I_{c2d} & -I_{c2q} \\ I_{c2q} & I_{c2d} \end{bmatrix} \begin{bmatrix} R_{c2} \\ X_{c2} \end{bmatrix} = \begin{bmatrix} U_{c2d} \\ U_{c2q} \end{bmatrix} \tag{19}$$

where U_{c2d} and U_{c2q}, and I_{c2d} and I_{c2q} are the d- and q-axis of $\dot{U}_{c2}$ and $\dot{I}_{c2}$, respectively.

To ensure the accuracy of online impedance prediction, the recursive least square estimation method is adopted. The weighted matrix W_k is set to the unit matrix, and it means that $w_k = 1(k = 1, 2, 3\ldots)$. The measurement matrix h_k can be obtained by (20).

$$h_k = \begin{bmatrix} I_{c2d\_k} & -I_{c2q\_k} \\ I_{c2q\_k} & I_{c2d\_k} \end{bmatrix} \tag{20}$$

The transient matrix P_k and K_k can be expressed as:

$$\begin{cases} P_1 = \left(h_1^T W_1 h_1\right)^{-1} = \dfrac{1}{I_{c2d\_1}^2 + I_{c2q\_1}^2} \begin{bmatrix} 1 & 0 \\ 0 & 1 \end{bmatrix} \\ P_{k+1} = P_k - P_k h_{k+1}^T \left[h_{k+1} P_k h_{k+1}^T + w_{k+1}^{-1}\right]^{-1} h_{k+1} P_k \end{cases} \tag{21}$$

$$K_k = P_k h_{k+1}^T \left[h_{k+1} P_k h_{k+1}^T + w_{k+1}^{-1}\right]^{-1} \tag{22}$$

Then, the estimated values can be expressed as (23).

$$\begin{cases} \begin{bmatrix} \hat{R}_{c2\_1} \\ \hat{X}_{c2\_1} \end{bmatrix} = \dfrac{1}{I_{c2d\_1}^2 + I_{c2q\_1}^2} \begin{bmatrix} I_{c2d\_1} & I_{c2q\_1} \\ -I_{c2q\_1} & I_{c2d\_1} \end{bmatrix} \begin{bmatrix} U_{c2d\_1} \\ U_{c2q\_1} \end{bmatrix} \\ \begin{bmatrix} \hat{R}_{c2\_k+1} \\ \hat{X}_{c2\_k+1} \end{bmatrix} = \begin{bmatrix} \hat{R}_{c2\_k} \\ \hat{X}_{c2\_k} \end{bmatrix} \\ +K_k \left(\begin{bmatrix} U_{c2d\_k+1} \\ U_{c2q\_k+1} \end{bmatrix} - h_{k+1} \begin{bmatrix} \hat{R}_{c2\_k} \\ \hat{X}_{c2\_k} \end{bmatrix} \right) \end{cases} \tag{23}$$

The PI controllers are used to regulate the voltage drop across the estimated impedance $\hat{R}_{c2}$ and $\hat{X}_{c2}$ according to the errors obtained from current feedback.

$$\begin{bmatrix} U_{c2d\_ref} \\ U_{c2q\_ref} \end{bmatrix} = G_{PI}(s) \begin{bmatrix} \hat{R}_{c2} & -\hat{X}_{c2} \\ \hat{X}_{c2} & \hat{R}_{c2} \end{bmatrix} \begin{bmatrix} I_{c2d\_ref} - I_{c2d} \\ I_{c2q\_ref} - I_{c2q} \end{bmatrix} \tag{24}$$

where U_{c2d_ref} and U_{c2q_ref}, I_{c2d_ref} and I_{c2q_ref} are d- and q-axis of reference values for $\dot{U}_{c2}$ and $\dot{I}_{c2}$, respectively.

The transfer function of the series converter can be simplified as (25) [36].

$$\begin{bmatrix} U_{c2d} \\ U_{c2q} \end{bmatrix} = \frac{1}{1 + T_v s} \begin{bmatrix} U_{c2d\_ref} \\ U_{c2q\_ref} \end{bmatrix} \tag{25}$$

The transfer function of the controlled system can be expressed as (26).

$$\begin{bmatrix} I_{c2d} \\ I_{c2q} \end{bmatrix} = \begin{bmatrix} R_{c2} + L_{c2}s & -\omega L_{c2} \\ \omega L_{c2} & R_{c2} + L_{c2}s \end{bmatrix}^{-1} \begin{bmatrix} U_{c2d} \\ U_{c2q} \end{bmatrix} \tag{26}$$

The control system can be expressed as

$$\begin{bmatrix} I_{c2d} \\ I_{c2q} \end{bmatrix} = G_o(s) \begin{bmatrix} I_{c2d\_ref} - I_{c2d} \\ I_{c2q\_ref} - I_{c2q} \end{bmatrix} \tag{27}$$

where $G_o(s)$ is the open-loop transfer function, and can be expressed as

$$\begin{cases} G_o(s) = \dfrac{G_{PI}(s)}{(1 + T_v s)\left[(R_{c2} + L_{c2}s)^2 + (\omega L_{c2})^2\right]} G_k(s) \\ G_k(s) = \begin{bmatrix} R_{c2} + L_{c2}s & \omega L_{c2} \\ -\omega L_{c2} & R_{c2} + L_{c2}s \end{bmatrix} \begin{bmatrix} \hat{R}_{c2} & -\hat{X}_{c2} \\ \hat{X}_{c2} & \hat{R}_{c2} \end{bmatrix} \end{cases} \tag{28}$$

When $\hat{R}_{c2} = R_{c2}$ and $\hat{X}_{c2} = \omega L_{c2}$, the transient matrix $G_k(s)$ can be simplified as (29).

$$G_k(s) = \begin{bmatrix} \hat{R}_{c2}^2 + \hat{X}_{c2}^2 + L_{c2}\hat{R}_{c2}s & -L_{c2}\hat{X}_{c2}s \\ L_{c2}\hat{X}_{c2}s & \hat{R}_{c2}^2 + \hat{X}_{c2}^2 + L_{c2}\hat{R}_{c2}s \end{bmatrix} \tag{29}$$

Then closed-loop frequency characteristics of control system can be obtained as shown in Fig. 10. In Fig. 10(a), when the impedance values change, the frequency characteristics within 100 rad/s almost do not change. For the frequency component above 100 rad/s, it also has strong anti-interference performance. Comparison of Fig. 10(a) and Fig. 10(b) illustrates that the performance of the proposed control strategy is better than that of the simple PI control strategy.

Hence, the outer-loop control strategy for the power flow process can be obtained, as shown in Fig. 11(a). During the power flow process, when SCLT system operates in the current mode, a PI controller for current regulation is added to the PI controller for voltage regulation, which forms the structure of inner-loop for voltage and outer-loop for current.

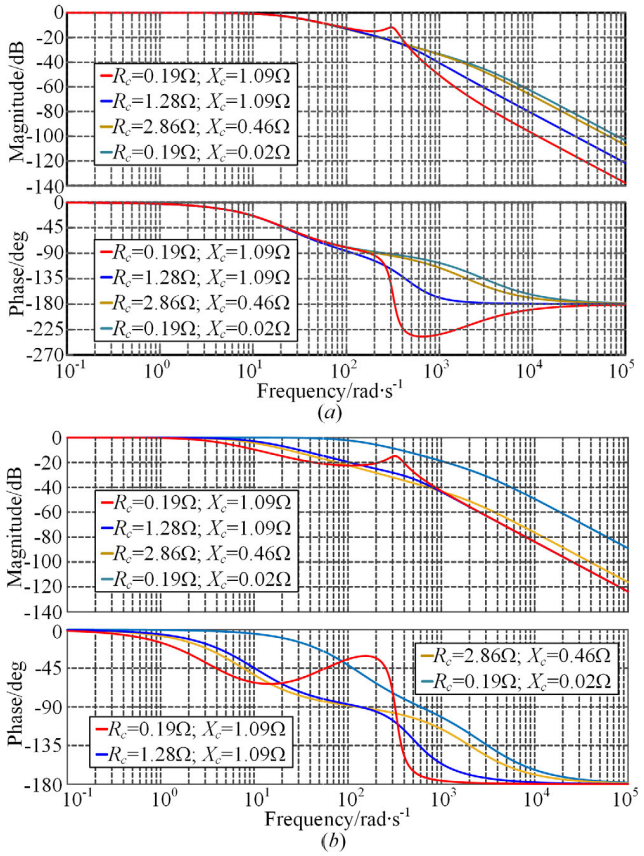

FIGURE 10. The Closed-loop frequency characteristics. (a) The proposed control system; (b) The simple PI control system.

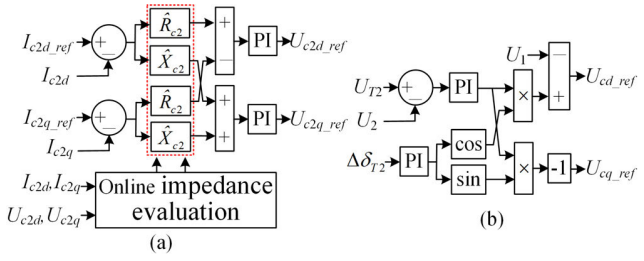

FIGURE 11. The outer loop control strategy of S-INV. (a) Power flow process. (b) Voltage regulation process.

3) VOLTAGE REGULATION PROCESS

The control objective of the voltage regulation process is in voltage mode to make the voltage $\dot{U}_2$ of bus II track the outlet voltage $\dot{U}_{T2}$ of transformer T2. However, the data about the voltage $\dot{U}_2$ and $\dot{U}_{T2}$ are measured and transmitted to SCLT prototype by RMU. The detailed data transmitted are two voltage RMS values U_2 and U_{T2}, and the phase angle difference $|\angle\dot{U}_{T2} - \angle\dot{U}_2|$ between two voltages, signed as $\Delta\delta_{T2}$.

During the voltage regulation process, the SCLT prototype is in voltage mode, and (30) can be obtained.

$$\dot{U}_2 = \dot{U}_1 + \dot{U}_c \tag{30}$$

The above can also be expressed as (31).

$$\begin{cases} U_{cd} = U_2\cos(\delta_2) - U_1 \\ U_{cq} = -U_2\sin(\delta_2) \end{cases} \tag{31}$$

where δ_2 is phase angle of $\dot{U}_2$.

The PI controllers are used to compensate for errors in amplitude and angle, shown as (32).

$$\begin{cases} U_2^* = G_{PI3}(s)\left(U_{2\_ref} - U_2\right) \\ \delta_2^* = G_{PI4}(s)\left(\delta_{2\_ref} - \delta_2\right) \end{cases} \tag{32}$$

where U_{2_ref} and δ_{2_ref} are the reference values of U_2 and δ_2, and U_2^* and δ_2^* are the control command values of U_2 and δ_2.

To make $\dot{U}_2$ track $\dot{U}_{T2}$, U_{2_ref} and δ_{2_ref} are set to U_{T2} and $(\Delta\delta_{T2} + \delta_2)$. Then, the d- and q-axis of reference values for $\dot{U}_c$ can be expressed as (33).

$$\begin{cases} U_{cd\_ref} = G_{PI4}(s)\left(U_{T2} - U_2\right)\cos\left(G_{PI4}(s)\Delta\delta_{T2}\right) - U_1 \\ U_{cq\_ref} = -G_{PI5}(s)\left(U_{T2} - U_2\right)\sin\left(G_{PI4}(s)\Delta\delta_{T2}\right) \end{cases} \tag{33}$$

The SCLT prototype is in voltage mode during the voltage regulation process, so the reference values I_{cd_ref} and I_{cq_ref} are set to I_{cd} and I_{cq}. Hence, the outer-loop control strategy for the voltage regulation process can be obtained, as shown in Fig. 11(b). Moreover, the time interval for data updates is 100 ms, which is five times the control cycle (20 ms). So, the PI parameters should be changed accordingly.

C. UPPER-LEVEL CONTROL STRATEGY

The upper-level control strategy is mainly responsible for the coordination of the four processes and the series-parallel modes. The upper-level control strategy for the four process of power supply transferring operation in single mode has been described in [17], and the control strategy for the power supply restoring operation is similar. The detailed is not descripted here. It is noted that the reference values in the SCLT prototype change linearly for field applications.

The SCLT prototype only runs for 60 seconds and then is in the bypass state. Therefore, the current sharing problem of S-INVs in parallel mode and the voltage sharing problem of S-INVs in series mode are not the main contradiction.

1) SERIES MODE

When the required single-phase injection voltage is greater than 70 V, multiple S-INVs can be operated in series. The typical scenario is that the wiring groups of the two distribution transformers are inconsistent, such as one is Δ/Yn-11 and the other is Δ/Δ. When the S-INVs operate in series, it is significant to coordinate their control strategies. The coordinated control strategy of two S-INVs in series mode is introduced below.

Before the start-up process, the primary DSP determines whether the operation mode and wiring are correct. Then the *CCB* in the S-INV near bus I (signed as S-INV I) is switched on, and the start-up process is performed. The modes of

TABLE 2. The modes of S-INVs in series-parallel mode.

Operation	Process	Series mode		Parallel mode	
		S-INV I	S-INV II	S-INV I	S-INV II
Transferring power supply operation	Assess	Voltage	Voltage	Voltage	Voltage
	Power flow	Voltage	Current	Current	Current
	Bypass	Voltage	Voltage	Current	Voltage
	Power self-circulation	Current	Current	Current	Current
Restoring power supply operation	Assess	Voltage	Voltage	Voltage	Voltage
	Power self-circulation	Current	Current	Current	Current
	Voltage regulation	Voltage	Voltage	Current	Voltage
	Power flow	Voltage	Current	Current	Current

S-INVs in series mode are shown in Table 2. During the access and power flow process of transferring power supply operation, the S-INV I is in voltage mode, which constantly compensates half of the phase angle difference. During all processes, the control strategy of S-INV near bus II (signed as S-INV II) is same as that of the S-INV in single mode. Form Table 2, the function of S-INV I in series mode is to reduce the phase angle difference for S-INV II's operation. During the power flow process, the S-INV II in the current mode should evaluate the impedance of the system, and control the line power.

2) PARALLEL MODE

The maximum transferred load current value of a single S-INV is 250 A, and S-INVs can be operated in parallel to meet the higher capacity requirements. As shown in Table 2, during the bypass process and the voltage regulation process, the SCLT prototype is in voltage mode to control $\dot{U}_2$ to track $\dot{U}_1$ or $\dot{U}_{T2}$. Hence, one of S-INVs (signed as S-INV I) is in current mode to constantly compensate half of the load currents, and the other (signed as S-INV II) is in voltage mode. Throughout all processes, the control strategy for S-INV II remains identical to that of the S-INV in single mode. From Table 2, the function of S-INV I in parallel mode is to take half of the transferred load current. It is noted that the S-INVs jointly regulate the transfer current and evaluate the impedance of the system together during the power flow process.

The internal impedance of S-INVs cannot be ignored when analyzing the online impedance evaluation technology of S-INVs in parallel mode. There will be circulating current between modules, which will affect the current information used in impedance evaluation, resulting in errors in the evaluated impedance. The equivalent circuit is shown in Fig. 12(a), and the Z_{Int-n} is the internal impedance of the n-th S-INV. Then the impedance Z_{c2}, $Z_{Int-\mathrm{I}}$ and $Z_{Int-\mathrm{II}}$ can

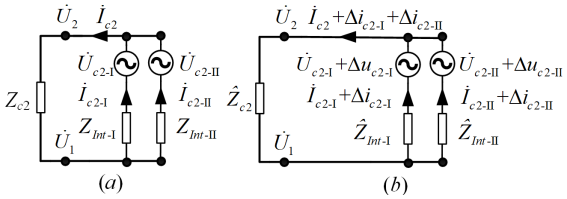

FIGURE 12. SCLT system in parallel mode. (a) Equivalent circuit; (b) Evaluated equivalent circuit.

be obtained by (34).

$$\begin{cases} \dot{I}_{c2} = \dot{I}_{c2\text{-I}} + \dot{I}_{c2\text{-II}} \\ \dot{I}_{c2}Z_{c2} = \dot{I}_{c2\text{-I}}Z_{Int\text{-I}} + \dot{U}_{c2\text{-I}} \\ \dot{I}_{c2}Z_{c2} = \dot{I}_{c2\text{-II}}Z_{Int\text{-II}} + \dot{U}_{c2\text{-II}} \end{cases} \tag{34}$$

The evaluated impedance values $\hat{Z}_{c2}$, $\hat{Z}_{Int-I}$ and $\hat{Z}_{Int-II}$ are obtained by P-REC, and sent to the S-INVs. Hence, the relationship between $\Delta u_{c2-\mathrm{I}}$, $\Delta i_{c2-\mathrm{I}}$, $\Delta u_{c2-\mathrm{I}}$ and $\Delta i_{c2-\mathrm{I}}$ can be expressed as (35).

$$\begin{cases} \Delta i_{c2\text{-I}} = \dfrac{\Delta u_{c2\text{-I}}}{\hat{Z}_{Int\text{-I}} + \hat{Z}_{Int\text{-II}} // \hat{Z}_{c2}} + \dfrac{\Delta u_{c2\text{-II}}}{\hat{Z}_{Int\text{-II}} + \hat{Z}_{Int\text{-I}} // \hat{Z}_{c2}} \cdot \dfrac{\hat{Z}_{c2}}{\hat{Z}_{Int\text{-II}} + \hat{Z}_{c2}} \\ \Delta i_{c2\text{-II}} = \dfrac{\Delta u_{c2\text{-II}}}{\hat{Z}_{Int\text{-II}} + \hat{Z}_{Int\text{-I}} // \hat{Z}_{c2}} + \dfrac{\Delta u_{c2\text{-I}}}{\hat{Z}_{Int\text{-I}} + \hat{Z}_{Int\text{-II}} // \hat{Z}_{c2}} \cdot \dfrac{\hat{Z}_{c2}}{\hat{Z}_{Int\text{-I}} + \hat{Z}_{c2}} \end{cases} \tag{35}$$

For the control strategy of the S-INVs, it is assumed that the slope of the current command value is consistent, and the $\Delta i_{c2-\mathrm{I}}$ is consistent with the $\Delta i_{c2-\mathrm{II}}$. The relationship between $\Delta u_{c2-\mathrm{I}}$ and $\Delta i_{c2-\mathrm{I}}$ can be expressed as (36). Then outer control strategy of S-INVs in parallel mode can be obtained.

$$\begin{cases} \Delta i_{c2\text{-I}} = \dfrac{\hat{Z}_{Int\text{-II}} + \hat{Z}_{c2}}{\hat{Z}_{Int\text{-II}}\left(\hat{Z}_{Int\text{-I}} + \hat{Z}_{c2}\right)} \Delta u_{c2\text{-I}} \\ \Delta i_{c2\text{-II}} = \dfrac{\hat{Z}_{Int\text{-I}} + \hat{Z}_{c2}}{\hat{Z}_{Int\text{-I}}\left(\hat{Z}_{Int\text{-II}} + \hat{Z}_{c2}\right)} \Delta u_{c2\text{-II}} \end{cases} \tag{36}$$

VI. LABORATORY TESTS AND RESULTS

The laboratory test environment and circuit diagrams are illustrated in Fig. 13. The voltage of bus I is obtained by transforming the grid voltage through the autotransformer, while the voltage of bus II is obtained by transforming the grid voltage through either a phase-shifting transformer or an isolated transformer. The phase-shifting transformer consists of an autotransformer and a transformer with a ratio of 4:1, and its phase-shifting angle is 11.4°. Moreover, the connection group of the isolated transformer is Δ/Yn-11, which causes a phase angle difference of 30°. The start-up unit is designed to suppress the inrush current of the transformers.

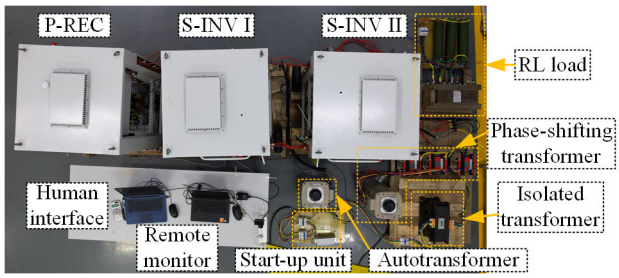

FIGURE 13. Laboratory tests field.

A. CASE A: LARGE CURRENT TEST DURING SELF-CIRCULATION PROCESS

It is difficult to achieve 250 A load current in the laboratory. Hence, the verification of the prototype's flow capacity is conducted solely through a large current test during the self-circulation process. During the large current test, the *PCB* and *CCB* are switched on, and the prototype generates compensation currents I_{c_abc}. The compensation currents I_{c_abc} circulate between the *PCB* and *CCB*. The time required for the reference values of compensation currents to rise from ZERO to 250 A is set to 5.0 seconds, and it takes about 5.5 seconds for the compensation currents to decrease from ZERO to 250 A, as shown in Fig. 14.

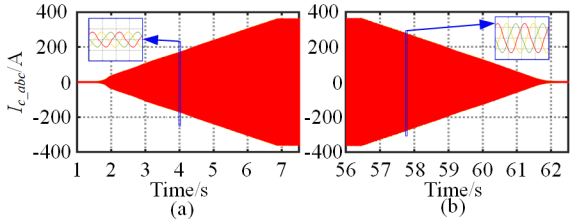

FIGURE 14. The compensation currents in case A.

To verify the thermal stability of magnetic components under large current conditions, three tests were carried out. Test I: At room temperature, the magnetic element is continuously injected with five times the rated current for 60 seconds. Test II: At room temperature, the magnetic element is continuously injected with the rated current until the heat balance condition. Test III: At the heat balance condition, the magnetic element is continuously injected with five times the rated current for 60 seconds. The temperature risk results of three test are shown in Table 3. Before the start-up process, all the magnetic components are at room temperature. After power supply transferring operation or power supply restoring operation, the temperature rise values of all the magnetic components are less than 26 K. This temperature increase remains within an acceptable range for engineering applications.

B. CASE B: TRANSFERRING POWER SUPPLY OPERATION

The RMS values of $\dot{U}_1$ and $\dot{U}_2$ are set to 237 V and 220 V, respectively. The phase-shifting transformer is used, and the phase angle difference of two bus bars is 11.4°. The loads

TABLE 3. The current test results of magnetic components.

Test	Temperature rise/K		
	Series transformers T_a, T_b, T_c	Filter inductance L_{fs}	Filter inductance L_{fp}
Test I	21.8	25.8	18.1
Test II	39.8	20.9	19.9
Test III	59.8	40.9	47.9

Note: The room temperature is 16.8°C.

are RL loads, which consist of 10 Ω resistance and 20 mH inductance each phase.

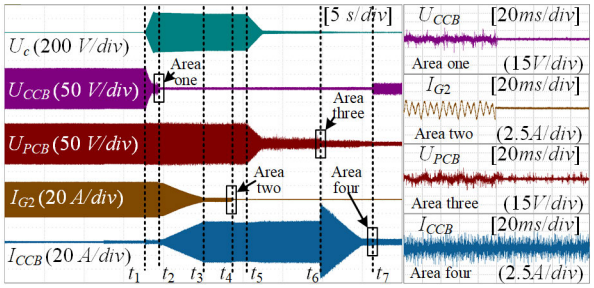

FIGURE 15. Voltages and currents in case B.

Fig. 15 illustrates the waveforms and results of voltages and currents. The U_{CCB} and U_{PCB} are the voltages at the ends of the *CCB* and *PCB*, respectively. I_{CCB} are the current flowing through the *CCB*. At t_1, the access process starts. At t_2, the *CCB* is switched on. At t_4, the *LCB* is switched off. At t_5, the quit process starts. At t_6, the *PCB* is switched on. At t_7, the *CCB* is switched off. It took about 28.4 seconds to complete a whole transferring power supply operation. The analysis of the detailed voltage and current waveforms presented in Fig. 15 shows that the main content of the voltage and current is harmonic content, rather than fundamental content, which verifies the effectiveness of the control strategy.

Fig. 16 illustrates the single-phase calculation results from test data. In Fig. 16, P_{CCB} and Q_{CCB}, P_{PCB} and Q_{PCB} are the active and reactive power flowing through the *CCB* and *PCB*, respectively. During the access process, the phase angle and voltage RMS of the voltage $\dot{U}_0$ are successively controlled to those of $\dot{U}_2$. At the moment the *CCB* is switched on, the voltage RMS and phase angle differences between $\dot{U}_2$ and $\dot{U}_0$ are 1.8 V and 0.1°, respectively. Next, the prototype enters the power flow process, and the current mode of S-INV is adopted. The active and reactive power $P_{G2} + jQ_{G2}$ are successively reduced from the recorded value to $(0.00 + j0.11)$ kVA under the control. During the power flow process, the estimated values of the impedance $\hat{R}_{c2}$ and $\hat{X}_{c2}$ are finally stabilized at $(1.28 + j1.09)$ Ω. During the quit process, the phase angle and voltage RMS of the voltage $\dot{U}_2$ are successively controlled from the recorded values to those of $\dot{U}_1$. At the moment the *PCB* is switched on, the

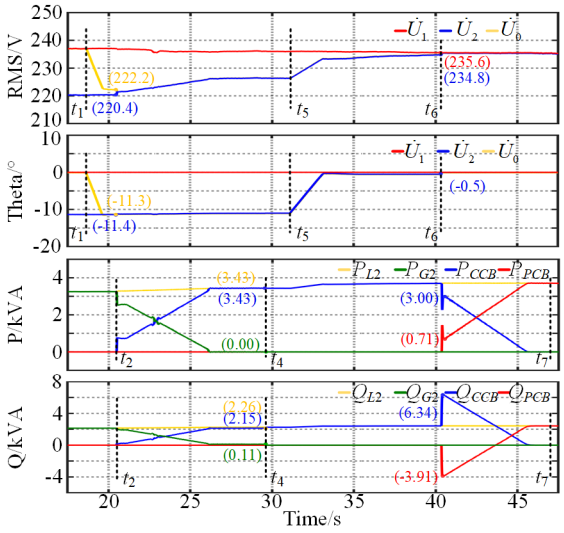

FIGURE 16. Single-phase voltages and power results in case B.

voltage RMS and phase angle differences between $\dot{U}_1$ and $\dot{U}_2$ are 0.8 V and 0.5°, respectively. During the power self-circulation process, the active and reactive power $P_{CCB} + jQ_{CCB}$ are reduced to ZERO through the implementation of current mode control. The estimated values of the impedance $\hat{R}_{c2}$ and $\hat{X}_{c2}$ are finally stabilized at $(0.19 + j0.02)\ \Omega$, which is the impedance of the *PCB* and its wire. The results in case B verify the effectiveness of control strategies employed for four processes and the seamless transitioning between them.

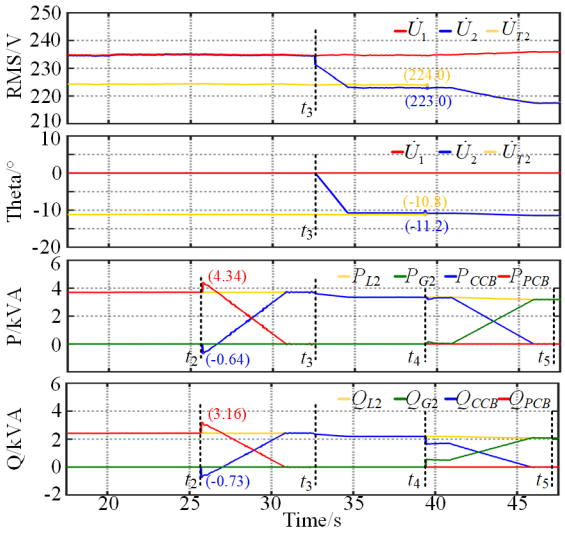

FIGURE 17. Single-phase voltage and power results in case C.

C. CASE C: POWER SUPPLY RESTORING OPERATION

Fig. 17 illustrates the single-phase power flow and the phase voltage RMS during the power flow process in case C. The $\dot{U}_{T2}$ is the outlet voltage of the phase-shifting transformer. At t_2, the *CCB* is switched on, and the power self-circulation process starts. At t_3, the *PCB* is switched off, and the voltage regulation process starts. At t_4, the *LCB* is switched on, and power flow process starts. At t_5, the *CCB* is switched off. It took about 22.0 seconds to complete the power supply restoring operation.

During the voltage regulation process, the phase angle and voltage RMS of the voltage $\dot{U}_2$ are successively controlled to those of $\dot{U}_{T2}$. At the moment the *LCB* is switched on, the voltage RMS and phase angle differences between $\dot{U}_2$ and $\dot{U}_{T2}$ are 1.0 V and 0.4°, respectively. The results have verified the effectiveness of the control strategy for the voltage regulation process. At the moment the *PCB* or *LCB* is switched off, the power flowing through the switch is near ZERO. The results in case C verify the feasibility of the control strategy implemented during power supply restoring operation.

D. CASE D: PARALLEL MODE OF S-INVs

The RMS values of $\dot{U}_1$ and $\dot{U}_2$ are set to 223 V and 235 V, respectively. The loads are RL loads, which consist of 10 Ω resistance and 20 mH inductance each phase.

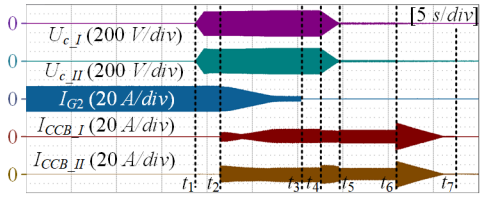

FIGURE 18. Voltages and currents in case D.

Fig. 18 illustrates the waveforms of voltages and currents in case D. The U_{c_I} and I_{CCB_I}, and U_{c_I} and I_{CCB_II} are the injected voltage and the currents flowing through the *CCB* of S-INV I and S-INV I, respectively. At t_1, S-INV I and S-INV II enter the access process. At t_2, the *CCB*s of S-INV I and S-INV II are switched on. At t_3, the *LCB* is switched off. At t_4, S-INV I and S-INV II enter the quit process. At t_6, the *PCB*s of S-INV I and S-INV II are switched on. At t_7, the *CCB*s of S-INV I and S-INV II are switched off. The main differences between the single mode and parallel mode are the power flow process and quit process. The control goal of each S-INV during the power flow process is to transfer half of the load current. During the quit process, S-INV II is in voltage mode, and S-INV I is in current mode.

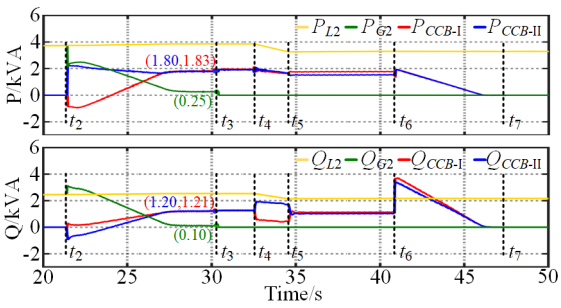

FIGURE 19. Single-phase power results in case D.

Fig. 19 illustrates the power flow in case D. The $P_{CCB-\mathrm{I}}$ and $Q_{CCB-\mathrm{I}}$, $P_{PCB-\mathrm{I}}$ and $Q_{PCB-\mathrm{I}}$, $P_{CCB-\mathrm{II}}$ and $Q_{CCB-\mathrm{II}}$, $P_{PCB-\mathrm{II}}$ and $Q_{PCB-\mathrm{II}}$ are the active and reactive power flowing through the *CCB* and *PCB* of S-INV I and S-INV II, respectively. At the end of the power flow process, the power transferred by S-INVs is $(1.80 + j1.20)$ kVA and $(1.83 + j1.21)$ kVA. During the quit process, the phase angle and voltage RMS of the voltage $\dot{U}_2$ are successively controlled to those of $\dot{U}_1$ under the control of S-INV II. During the voltage control of S-INV II, the current control of S-INV I is differential regulation. The power control strategy of parallel mode meets the demand of power sharing, and the strategy's effectiveness is verified by the results.

E. CASE E: SERIES MODE OF S-INVs

The RMS values of $\dot{U}_1$ and $\dot{U}_2$ are set to 225 V and 219 V. The isolated transformer is used, and the phase angle difference of two bus bars is 30°. The loads are RL loads, and consist of 20 Ω resistance and 20 mH inductance each phase.

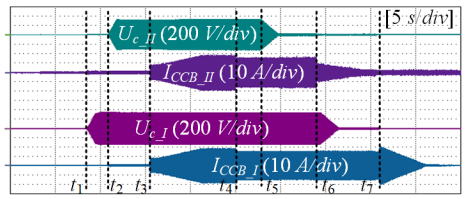

FIGURE 20. Voltages and currents in case E.

Fig. 20 illustrates the voltages and currents in case E. At t_1, the access process of S-INV I starts. At t_2, the access process of S-INV I starts. At t_3, the *CCB* is switched on. At t_4, the *LCB* is switched on. At t_5, the bypass process of S-INV II starts. At t_6, the *PCB* of S-INV II is switched on, and then the bypass process of S-INV II starts. At t_7, the *PCB* of S-INV I is switched on.

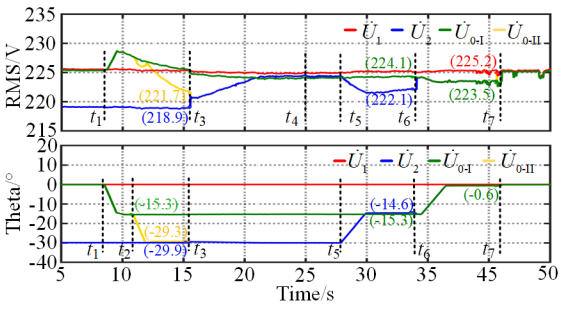

FIGURE 21. Single-phase voltage results in case E.

In Fig. 21, $\dot{U}_{0-\mathrm{I}}$ and $\dot{U}_{0-\mathrm{II}}$ are the voltage after compensation of S-INV I and S-INV II, respectively. At the moment the CCB is switched on, the phase angle compensated by S-INV I is 15.3°, and the voltage RMS and phase angle differences between $\dot{U}_2$ and $\dot{U}_0$ are 2.8 V and 0.6°, respectively. At the moment the PCB of S-INV I is switched on, the voltage RMS and phase angle differences between $\dot{U}_{0-\mathrm{I}}$ and $\dot{U}_2$ are 2.0 V and 0.7°, respectively. At the moment the PCB of S-INV II is switched on, the voltage RMS and phase angle differences between $\dot{U}_1$ and $\dot{U}_{0-\mathrm{I}}$ are 1.7 V and 0.6°, respectively. All the error of voltage RMS and phase angle are still in acceptable range. During the power flow process, the estimated values of the impedance $\hat{R}_{c2}$ and $\hat{X}_{c2}$ are stabilized at $(2.86 + j0.46)$ Ω. The coordinated control strategy of series mode meets the demand of voltage sharing, and the effectiveness of control strategies based on online impedance estimation is verified again.

VII. CONCLUSION

To further improve the power supply reliability, a seamless closed-loop load transfer (SCLT) scheme was proposed based on series compensation technology. For the efficient utilization, the SCLT prototype is designed with high mobility. To promote the field application of the SCLT prototype, the following were proposed: 1) Putting forward the control strategy based on the online impedance estimation method to ensure the effectiveness of SCLT prototype in variable scenarios. 2) Utilizing the short-term overload capacity of magnetic components to reduce the volume and weight. 3) Employing modular design to reduce the volume of an individual cabinet, while implementing the modules' series-parallel mode to meet the voltage and capacity requirements of variable scenarios. A mobile SCLT prototype has been developed and tested, demonstrating excellent transient and dynamic performance. The test results verified the effectiveness of the control strategy and the engineering feasibility of the prototype. The next step is the SCLT prototype's field applications.

REFERENCES

[1] T. Strasser, F. Andrén, J. Kathan, C. Cecati, C. Buccella, P. Siano, P. Leitão, G. Zhabelova, V. Vyatkin, P. Vrba, and V. Mařík, "A review of architectures and concepts for intelligence in future electric energy systems," *IEEE Trans. Ind. Electron.*, vol. 62, no. 4, pp. 2424–2438, Apr. 2015.

[2] M. E. Honarmand, V. Hosseinnezhad, B. Hayes, M. Shafie-Khah, and P. Siano, "An overview of demand response: From its origins to the smart energy community," *IEEE Access*, vol. 9, pp. 96851–96876, 2021.

[3] K. Kawahara, H. Sasaki, J. Kubokawa, H. Asahara, and K. Sugiyama, "A proposal of a supporting expert system for outage planning of electric power facilities retaining high power supply reliability. II. Knowledge processing and simulation results," *IEEE Trans. Power Syst.*, vol. 13, no. 4, pp. 1459–1465, Nov. 1998.

[4] C. Singh, N. Gubbala, and N. Gubbala, "Reliability analysis of electric supply including standby generators and an uninterruptible power supply system," *IEEE Trans. Ind. Appl.*, vol. 30, no. 5, pp. 1298–1302, Sep. 1994.

[5] X. Guo and S. Ma, "Reliability assessment of the external power supply in electrified railways with weak power sources," *IEEE Access*, vol. 9, pp. 117608–117614, 2021.

[6] X. Wang, P. Lu, Y. Ye, Y. Zhang, G. Cheng, and H. Li, "An intelligent low-voltage contact box based on closed-loop power supply technology," *Autom. Appl.*, vol. 8, pp. 112–115, Aug. 2020.

[7] F. M. Rodrigues, L. R. Araujo, and D. R. R. Penido, "A method to improve distribution system reliability using available mobile generators," *IEEE Syst. J.*, vol. 15, no. 3, pp. 4635–4643, Sep. 2021.

[8] M. K. Metwaly and J. Teh, "Probabilistic peak demand matching by battery energy storage alongside dynamic thermal ratings and demand response for enhanced network reliability," *IEEE Access*, vol. 8, pp. 181547–181559, 2020.

[9] J. Li, A. Zhan, X. Liu, Q. Lin, and X. Zhang, "Scheme and optimization strategy for low-voltage uninterrupted operation," *Shandong Electr. Power*, vol. 48, no. 4, pp. 25–30, Apr. 2021.

[10] J. Liu, Q. Sun, X. Zhang, and Z. Zhang, "Analysis on and criteria for loop closing operation for distribution grids," *Autom. Electr. Power Syst.*, vol. 38, no. 11, pp. 130–135, Jun. 2014.
[11] J. Li, X. Wang, C. Xie, J. Han, C. Mao, X. Liu, D. Wang, Y. Zhang, Z. Guan, and X. Zhang, "A novel method for seamless closed-loop load transfer in radial distribution networks," *IEEE Trans. Ind. Appl.*, vol. 59, no. 2, pp. 2254–2265, Mar. 2023.
[12] R. Vargas, L. H. Macedo, J. M. Home-Ortiz, and R. Romero, "Optimal restoration of distribution systems considering temporary closed-loop operation," *IEEE Syst. J.*, vol. 15, no. 4, pp. 5483–5494, Dec. 2021.
[13] H. Tang, "Research on loop-closing risk assessment for 10 kV distribution network," M.S. thesis, Electron. Eng., South China Univ. Technol., Guangzhou, China, 2012.
[14] X. Yan, W. Peng, Y. Wang, W. Aslam, C. Shao, and T. Li, "Flexible loop closing control method for an active distribution network based on dual rotary phase shifting transformers," *IET Gener., Transmiss. Distrib.*, vol. 16, no. 20, pp. 4204–4214, Aug. 2022.
[15] Y. Yang, J. Tang, C. Niu, Z. Xu, and C. Zhao, "Coupling characteristic and control strategy for loop closing device based on improved phase shifting transformer under three-phase asymmetry condition," *Autom. Electr. Power Syst.*, vol. 46, no. 14, pp. 158–168, Jul. 2022.
[16] J. Li, H. Jie, C. Xie, X. Zhang, X. Zhang, and D. Wang, "Solutions for seamless closed-loop load transfer of low-voltage distribution network in multiple application scenarios," *Electr. Power Construct.*, vol. 43, no. 7, pp. 113–120, Jul. 2022.
[17] C. Xie, Z. Guan, J. Li, C. Mao, D. Wang, J. Li, X. Wang, Z. Liu, Y. Zhang, and Y. Qi, "Modeling and simulation of a load transfer controller for uninterrupted operation of low-voltage distribution grids," in *Proc. IEEE 4th Int. Electr. Energy Conf. (CIEEC)*, Wuhan, China, May 2021, pp. 1–6.
[18] J. Li, S. Lin, J. Li, Y. Luo, C. Mao, H. Li, D. Wang, W. Peng, and Z. Guan, "Risk assessment method of loop closing operation in low-voltage distribution network based on fuzzy comprehensive evaluation," *Energy Rep.*, vol. 9, pp. 312–319, May 2023.
[19] M. Lu, M. Qin, J. Kacetl, E. Suresh, T. Long, and S. M. Goetz, "A novel direct-injection universal power flow and quality control circuit," *IEEE J. Emerg. Sel. Topics Power Electron.*, vol. 11, no. 6, pp. 6028–6041, Dec. 2023.
[20] L. Liu, Y. Kang, J. Zhang, P. Zhu, and X. Liu, "Control scheme and implement of a unified power flow controller," *Proc. CSEE*, vol. 26, no. 10, pp. 114–119, May 2006.
[21] S. Yang, Y. Liu, X. Wang, D. Gunasekaran, U. Karki, and F. Z. Peng, "Modulation and control of transformerless UPFC," *IEEE Trans. Power Electron.*, vol. 31, no. 2, pp. 1050–1063, Feb. 2016.
[22] P. Song, "Research on control and optimization of power system with UPFC," Ph.D. thesis, Electron. Eng., Zhejiang Univ., Zhejiang, China, Jul. 2018.
[23] M. E. A. Farrag and G. A. Putrus, "Design of an adaptive neurofuzzy inference control system for the unified power-flow controller," *IEEE Trans. Power Del.*, vol. 27, no. 1, pp. 53–61, Jan. 2012.
[24] Q. Cheng, Y. Cheng, Y. Cheng, and L. Zhang, "Backstepping sliding mode control strategy for unified power flow controller based on MMC," *Power Grid Anal. Study*, vol. 51, no. 6, pp. 41–48, Jun. 2023.
[25] F. M. Albatsh, S. Mekhilef, S. Ahmad, and H. Mokhlis, "Fuzzy-logic-based UPFC and laboratory prototype validation for dynamic power flow control in transmission lines," *IEEE Trans. Ind. Electron.*, vol. 64, no. 12, pp. 9538–9548, Dec. 2017.
[26] Y. Lu, G. Xiao, X. Wang, F. Blaabjerg, and D. Lu, "Control strategy for single-phase transformerless three-leg unified power quality conditioner based on space vector modulation," *IEEE Trans. Power Electron.*, vol. 31, no. 4, pp. 2840–2849, Apr. 2016.
[27] R. M. Abdalaal and C. N. M. Ho, "System modeling and stability analysis of single-phase transformerless UPQC integrated input grid voltage regulation," *IEEE J. Emerg. Sel. Topics Ind. Electron.*, vol. 3, no. 3, pp. 670–682, Jul. 2022.
[28] M. M. Khan, J. Nebhen, and H. Rahman, "Research on variable frequency transformer: A smart power transmission technology," *IEEE Access*, vol. 9, pp. 105588–105605, 2021.
[29] M. A. Elsaharty, A. Luna, J. I. Candela, and P. Rodriguez, "A unified power flow controller using a power electronics integrated transformer," *IEEE Trans. Power Del.*, vol. 34, no. 3, pp. 828–839, Jun. 2019.
[30] A. Ingalalli and S. Kamalasadan, "A novel sequence-based unified control architecture for multiple inverter modes of operation in unbalanced distribution system," *IEEE Trans. Power Del.*, vol. 38, no. 2, pp. 1182–1196, Apr. 2023.
[31] H. Cheng, "Calculation of allowable overload time of dry-type transformer," *Transformer*, vol. 44, no. 2, pp. 18–21, 2007.
[32] L. Li, Q. Cheng, and L. Zhou, "Transformer design calculation," in *Design Principle of Electromagnetic Device*, 2nd ed. Beijing, China: China Electr. Power Press, 2017, pp. 42–82.
[33] G. Xu, "Convection heat transfer principle, convection heat transfer calculation, thermal radiation basis, and radiation heat transfer calculation," in *Engineering Heat Transfer*, 1st ed. Beijing, China: China Electr. Power Press, 2011, pp. 66–167.
[34] H. Jiang, Q. Xu, and H. You, "Study on temperature rise theory and calculation method of dry-type transformer," *Transformer*, vol. 53, no. 1, pp. 14–18, Jan. 2016.
[35] J. Biernacki and D. Czarkowski, "High frequency transformer modeling," in *Proc. ISCAS*, Sydney, NSW, Australia, 2001, pp. 676–679.
[36] L. Liu, Y. Kang, J. Cheng, and P. Zhu, "Cross-coupling control scheme and performance analysis for power flow control of UPFC," *Proc. CSEE*, vol. 27, no. 10, pp. 42–48, Apr. 2007.
[37] S. Wang, L. Jing, Y. Zhao, H. R. Wickramasinghe, X. Wu, and G. Konstantinou, "Operation of unified power flow controller as virtual synchronous generator," *IEEE Access*, vol. 8, pp. 162569–162580, 2020.

ZHITAO GUAN received the B.S. degree in electrical engineering from the Huazhong University of Science and Technology, Wuhan, China, in 2019, where he is currently pursuing the Ph.D. degree.

His research interests include power system operations and control, the application of power electronic technology in power systems, and power system control.

PENGFEI TANG received the B.S. degree from the Department of Electrical Engineering, Huazhong University of Science and Technology, Wuhan, China, in 2022, where he is currently pursuing the Ph.D. degree.

His research interest includes the application of power electronic technology in power systems.

CHENGXIONG MAO (Fellow, IEEE) received the B.S., M.S., and Ph.D. degrees in electrical engineering from the Huazhong University of Science and Technology (HUST), in 1984, 1987, and 1991, respectively.

He is currently a Professor with HUST. His research interests include power system operation and control and the applications of high-power electronic technology to power systems.

DAN WANG (Senior Member, IEEE) received the B.S., M.S., and Ph.D. degrees in electrical engineering from the Huazhong University of Science and Technology (HUST), in 1999, 2002, and 2006, respectively.

He is currently a Professor with HUST. His research interests include power system operations and control, power conditioning, and grid-connection of energy sources.

LEXIANG WANG received the B.S. degree from the School of Energy and Power Engineering, Huazhong University of Science and Technology (HUST), where he is currently pursuing the master's degree.

His research interest includes power system operations and control.

WENGE LIU received the B.S. degree in electrical engineering from Hohai University, Nanjing, China, in 2021. He is currently pursuing the master's degree with the Huazhong University of Science and Technology.

His research interest includes power system operation and control.

MIAOMIAO DU received the B.S. degree in electrical engineering from Wuhan University, in 2021. She is currently pursuing the master's degree with the Huazhong University of Science and Technology.

Her research interest includes power system operation and control.

JUNLIN LI received the B.S. and M.S. degrees in electrical engineering from the Huazhong University of Science and Technology, in 2014 and 2017, respectively.

He is currently with the Guangzhou Power Supply Bureau, engaged in distribution network planning. His research interests include the reliability management, operation, and the maintenance of the distribution networks.

XIAOCONG WANG received the B.S. degree from the South China University of Technology, Guangzhou, China, in 2013, and the M.S. degree from the University of Perpetual Help System DALTA, Las Piñas, Philippines, in 2022.

He is currently with the Guangzhou Power Supply Bureau, engaged in the operation monitoring and production command of the distribution networks. His research interest includes the operation and planning of the distribution networks.